


Tuning the tilt of the Dirac cone by atomic manipulations in 8Pmmn borophene

Yasin Yekta¹, Hanif Hadipour² & Seyed Akbar Jafari^{1,3}  [✉]

Two dimensional quantum materials possessing Dirac cones in their spectrum are fascinating due to their emergent low-energy Dirac fermions. In 8Pmmn borophene the Dirac cone is furthermore tilted, which is a proxy for spacetime geometry, since the future light-cone depends on the underlying metric. Therefore it is important to understand the microscopic origin of the tilt. Here, based on ab-initio calculations, we decipher the atomistic mechanism of the formation of tilt. First, nearest-neighbor hopping on a buckled honeycomb lattice forms an upright Dirac cone. Then, the difference in the renormalized anisotropic second-neighbor hopping, formed by virtual hoppings on one-dimensional chains of atoms, tilts the Dirac cone. We construct an accurate tight-binding model on honeycomb graph for analytical investigation, and we find that substitution of certain boron atoms by carbon provides a way to change the tilt of the cone.

¹Department of Physics, Sharif University of Technology, Tehran 11155-9161, Iran. ²Department of Physics, University of Guilan, Rasht 41335-1914, Iran. ³Physics of Quantum Materials Group, School of Physical Sciences, University of Kent, Canterbury CT2 7NZ, UK. ✉email: jafari@physics.sharif.edu

The marriage between the mathematical concept of “topology” and quantum materials lead to the birth of “topological materials” and developments that followed afterwards. Can the (local) “geometry” play a similar role in combination with quantum materials? In the same way that the appearance of Dirac fermions in graphene and other Dirac materials can be attributed to an emergent Minkowski spacetime structure at distances much larger than the atomic distances, quantum materials with “tilted Dirac cone” can be naturally associated with an emergent spacetime (not merely the space) metric. In these class of materials the tilt is a proxy to spacetime geometry. We use *Geometric Quantum Material* (GQM) to refer to them.

Every periodic structure in quantum condensed matter is mounted on a mathematical object called lattice. Irrespective of which atoms one wishes to place on the sites of a given lattice, they come in 230 possible structures¹. The presence of lattice breaks translation and rotation, and some times parity and/or time reversal invariance of the vacuum². The lattice therefore breaks the Poincaré group³ thereby the connection between spin and statistics of the particles is lost and therefore one may have fermions with integer spin that is enforced by the irreducible representations of its space group (SG)⁴.

Is there any other interesting consequence that can be associated with the underlying SG? To set the stage for answering this question, let us start by a simple, but profound observation²: Consider a simple quantum mechanical hopping process on a lattice and think about the wave equation in the continuum limit. On the square lattice the Hamiltonian becomes $-\hbar^2\nabla^2/(2m^*)$, while on the honeycomb lattice it becomes $i\hbar v_F\sigma\cdot\nabla$, namely the massless Dirac Hamiltonian⁵. Therefore despite that in the continuum limit, the lattice spacing is immaterial, but still remnants of the microscopic symmetries of the pertinent SG are manifested in the long-distance behavior and decide whether the structure of the ensuing spacetime is Galilean or Minkowskian. This can be regarded as an example of metamorphosis of atomic scale symmetry to a long-distance geometrical structure. The duality between atomic scale SG symmetry and long distance geometry is central to understand the geometric structure in GQMs.

What is the microscopic mechanism of such a duality between the microscopic structure and the long-distance (low-energy) characteristics in more complicated lattice structures? The long-distance behavior of interest for us is the tilted Dirac cone band whose Hamiltonian is $\alpha(\sigma\cdot\nabla) + \sigma_0\zeta\cdot\nabla$ ^{6–11} where σ_0 is the 2×2 unit matrix. A vector-looking quantity ζ here determines the tilt of the Dirac cone. But at a much deeper level, it can be encoded into an emergent spacetime metric $ds^2 = -(v_F dt)^2 + (dx - \zeta v_F dt)^2$ ^{9,10,12–17}, where v_F is the Fermi velocity. Therefore the tilt of a Dirac cone is actually a proxy for an emergent solid-state spacetime structure. Since the density of states is enhanced by a $1/\sqrt{1-\zeta^2}$, the tilted Dirac cone materials can generically give stronger responses to external stimuli. This enhancement nicely fits into spacetime description as a “redshift” factor¹⁸. Therefore it is crucial to understand the atomistic mechanism of the formation of the tilt in order to utilize it.

In this work we decipher the microscopic mechanism that determines the tilt parameter ζ . For this purpose we focus on the SG number 59 that describes the 8Pmmn structure of borophene^{9,19,20}. The tilted Dirac cone has been experimentally observed in the so called χ_3 structure of borophene²¹. The logic employed here is generic and is applicable to other SGs, and can even be used to discover further examples of GQM. We show that in this structure, the low-energy and high-energy degrees of freedom are nicely separated into two sublattices denoted by gray and teal circles in Fig. 1a, respectively. When the high energy sites available in this particular SG are integrated out, the underlying

honeycomb lattice will be promoted to a “honeycomb graph”. Therefore the molecular orbitals play significant role in attaching new “graph edges” to the simple underlying honeycomb lattice. As we will see, this graph has the ability to lead to a controllable tilt and hence a tunable spacetime structure in the long distance. On such a graph, even if instead of fermions one places circuit elements, again a tilted Dirac cone can be obtained²². Therefore in addition to GQMs, the circuits can also emulate interesting spacetime structures with a larger degree of tunability.

Results

Protection of the Dirac node. The relevant orbitals in the boron (as well as C) atom are $2p$ orbitals. The possibility of formation of sp^2 and sp^3 hybridization establishes the honeycomb lattice²³, and structures such as 8Pmmn that involve buckled honeycomb networks as natural lattices for these atoms. As can be seen in Fig. 1a, there is a backbone (buckled) honeycomb sub-lattice denoted with gray circles that are called inner (I) sites. The rest of the lattice sites are called ridge (R) sites and are denoted by teal circles. First principle calculations indicate that the resulting Dirac cone is tilted^{24,25} which is shown as red (low-energy) band in Fig. 1b and the three dimensional reconstruction of the band structure is shown in panel (c). The first thing that the 8Pmmn SG implies about the tilted Dirac cone is that on the MX and MY lines in the border of the Brillouin zone (BZ) of Fig. 1d, two bands “stick together” (as Kittel puts it²⁶) where the two-dimensional irreducible representations are protected by non-symmorphic elements²⁶. Then the compatibility relations gives the qualitative band picture of cat’s cradle shape²⁷ shown in panel (d). For pedagogical details of the derivation of this figure with group theory methods see the Supplementary Note 1, or more extended version of this paper²⁸.

Of course the protection of the tilted Dirac cone by the underlying SG is interesting, but it is not essential for the main purpose of this paper, namely the “tilt” of the Dirac cone. The symmetry considerations do not explain why and how the tilt parameter ζ is formed. In order to “manipulate” the tilt of the Dirac cone at will, one needs a microscopically detailed understanding of the root cause of formation of tilt in the Dirac cone. To achieve this, we need to identify the low-energy degrees of freedom that give rise to the tilted Dirac cone dispersion. For this purpose in Fig. 1e we have plotted an orbital projected representation of the band structure that resolves the contribution of atoms 2 (I) and 5 (R). As can be seen, the dominant contributions to the tilted Dirac dispersion comes from the p_z orbitals of the I atoms (top left plot in panel (e)). The R atoms also contribute via their p_z and p_x orbitals (bottom left and center). The remaining two boxes on the top row indicate little contributions from the p_x and p_y orbitals of the I atoms that arises from the buckling of the honeycomb sublattice.

In Fig. 2a we have labeled atomic hoppings paths with green and red dashed lines that connect I sites by virtual hoppings through R sites. There is only first neighbor direct hopping between the I sites denoted by black arrows. The appropriate atomic orbitals involved in forming the above microscopic t_{ij} hoppings can be extracted from the density functional theory (DFT) calculation. Working in a gauge that all t_{ij} ’s are real, the hermiticity implies $t_{ij} = t_{ji}$. Fig. 2b depicts the BZ of original 8Pmmn lattice. The insight from the projected bands in the left and center columns in the second row of Fig. 1e is that both p_x and p_z orbitals of the R atoms are of comparable importance and must be incorporated into the atomic scale computation of the t_{65} (dark green) and t_{87} (light green). Similarly the first column of Fig. 1e suggests that the p_z orbitals of R and I atoms dominate in $t_{36} = t_{35}$ hopping process. Table 1 shows the calculated values

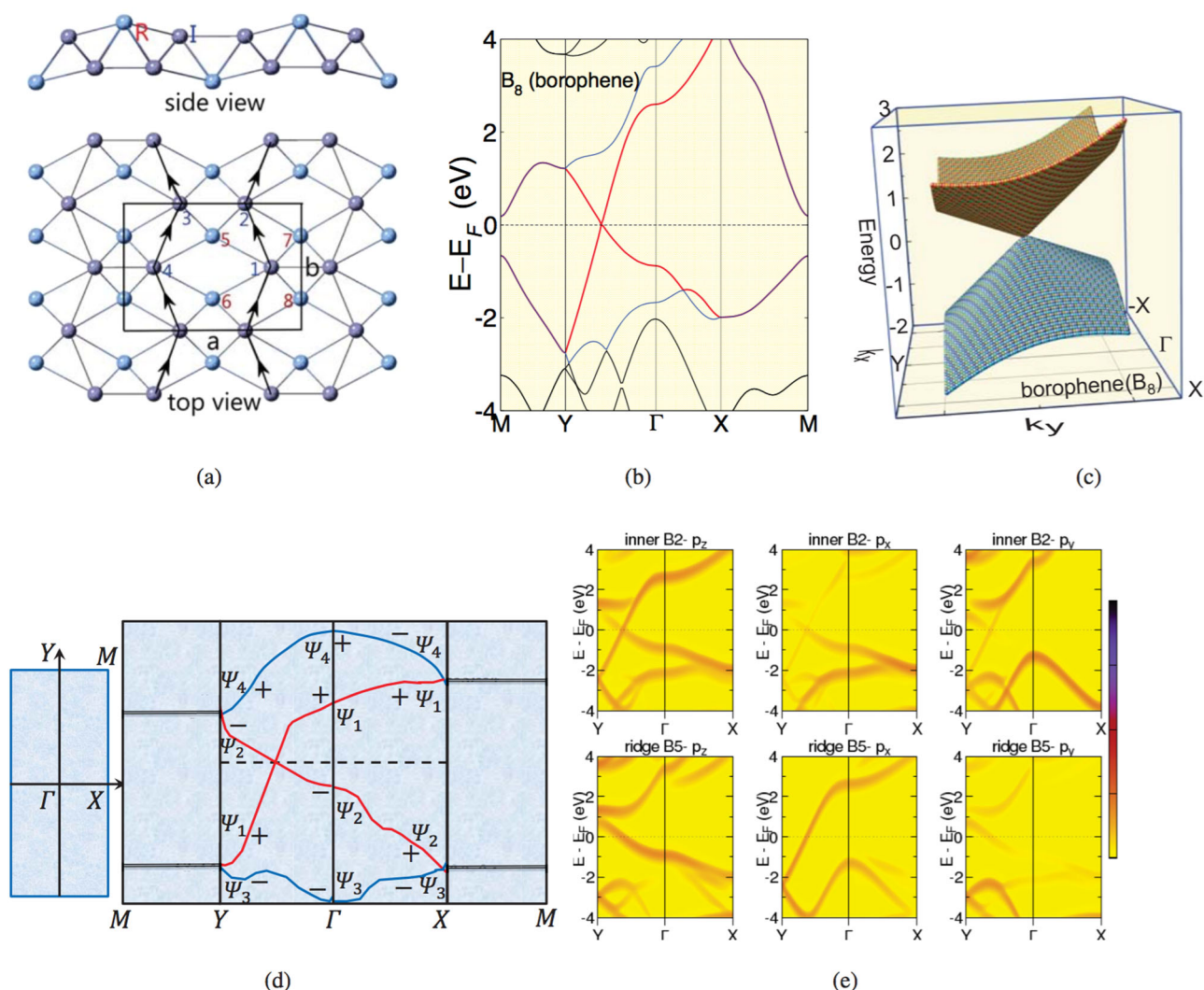


Fig. 1 Electronic structure of pure 8 Pmmn borophene. **a** Top and side view of crystal structure of 8 Pmmn borophene. The gray and faint teal circles denote inner (I) and ridge (R) boron atoms, respectively. **b** Density functional theory with Perdew-Burke-Ernzerhof parameterization (DFT-PBE) band structure of pristine 8 Pmmn borophene and **(c)** its three dimensional reconstruction. **d** First Brillouin zone and decomposition of elementary band representation the 8 Pmmn group. The \pm are the eigenvalues of \tilde{C}_{2x} , and \tilde{C}_{2y} operations at high-symmetry points. **e** The orbital-projected band structures for two atoms of 8 Pmmn borophene based on DFT-PBE. The Fermi energy (E_F) is set to the zero energy.

of these hopping parameters for pristine borophene (B_8) and C-doped borophene B_6C_2 using Wannier function^{29,30}. The purpose of substituting C for B is to study its effect in the tilt of the Dirac cone. The substituted carbon dimers are placed in R and I positions, respectively. Using these parameters one can reconstruct the ab initio bands with four p_z orbitals of four inner sites, and eight p_x and p_z orbitals of ridge sites. The nice coincidence of the original DFT bands with Wannier-interpolated bands in Supplementary Fig. 9 shows that the obtained t_{ij} values are reliable and the used atomic orbitals are adequate.

Although such an atomic picture might be satisfactory if one wishes to focus on the low-energy features of the tilted Dirac cone around the Fermi surface, but still working with a 12-band Hamiltonian is neither convenient, nor the essential long-range physics depends on so many short-distance details. To achieve an effective two-band model (for more details see Supplementary Note 2), we need to decimate the 8Pmmn lattice into an effective honeycomb graph shown in Fig. 2c where two possible ways of representing its BZ are depicted in Fig. 2d. On such a coarse-grained lattice, the virtual atomic hopping paths will be replaced by effective hoppings of the same color in panel (c). The connection

between these effective hoppings and atomic hoppings t_{ij} is a nice example of renormalization that will be discussed now.

Renormalization via molecular orbitals. Anderson in his book maintains that renormalization is one of the pillars of condensed matter physics³¹. In this section we will show that the same concept is encoded into a local quantum chemistry of the 8Pmmn borophene. Since we are not interested in higher energy features that take place away from the tilted Dirac node, we build an effective picture based on Fig. 2c where the “effective” hoppings must be evaluated from the atomic scale data in the upper part of Table 1. The low-energy degrees of freedom are dominated by the p_z orbitals of the I sites. So we decimate the 8Pmmn lattice by elimination of the R sites. In doing so, the effective coarse-grained system becomes the honeycomb graph in Fig. 2c. The nearest neighbor hoppings denoted by black arrows take place within the low-energy subspace and are responsible for the formation of a parent Dirac cone from the p_z orbitals of the I sites. Slight anisotropy in the black arrows is known to shift the location of the Dirac cone^{32,33} within the rhombus BZ of panel (d) that we

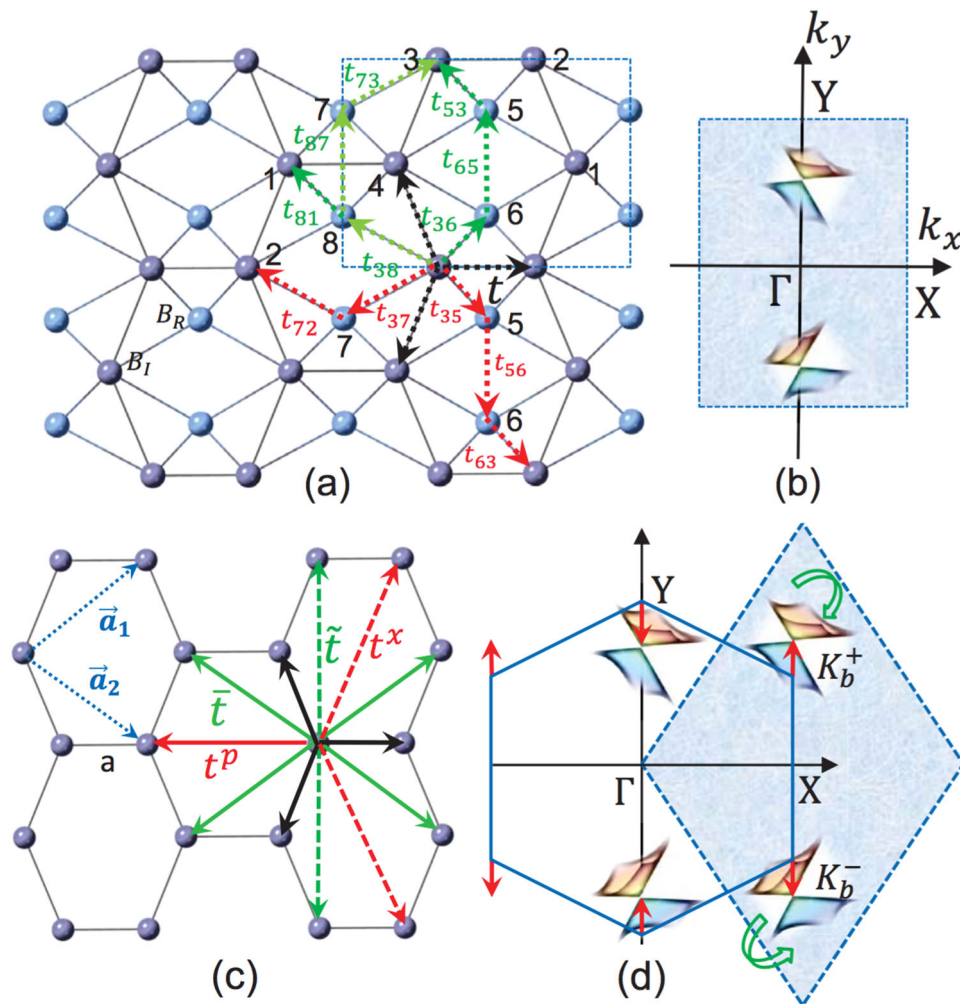


Fig. 2 Coarse graining of 8Pmmn lattice into honeycomb graph. **a** The lattice structure, unit cell, and hopping processes in the 8 Pmmn lattice. Inner sites (I) are denoted by teal circles while the ridge (R) sites are denoted by gray circles. **b** The Brillouin zone of 8 Pmmn lattice with two tilted Dirac cones. **c** The “effective” honeycomb graph of I atoms (low-energy degrees of freedom) obtained by elimination of R sites from the 8 Pmmn lattice. **d** two representations (rhombus and hexagonal) of the Brillouin zone of the effective honeycomb structure. The effective second/third neighbor hoppings (green/red) in (c) arise from the corresponding hopping path in (a) via the process of renormalization (see the section on Renormalization via molecular orbitals). As indicated in (d), the red (third neighbor) hopping shifts the Dirac cone, while the green (second neighbor) hoppings tilt the cone.

Table 1 Atomic and renormalized hoppings (in eV) for borophene and carbon-substituted borophene.

(atomic)	t_{36}	t_{65}	t_{53}	t_{81}	t_{38}	t_{37}	t_{72}	t_{78}
pure borophene B_8	2.09	-2.66	2.09	2.09	-1.87	-1.87	-1.87	-2.54
B_6C_2 -I-[C2&C3]	1.93	-2.52	1.96	1.92	-1.52	-1.52	-1.55	-2.34
B_6C_2 -R-[C5&C6]	2.14	-2.33	2.12	2.15	-2.23	-2.21	-2.20	-2.43
(renormalized)	t	t^p	t^x	\tilde{t}	\bar{t}	ζ_y	k_D/k_Y	ζ_y^{DFT}
pure borophene B_8	-2.21	-2.36	-1.07	-1.99	-2.51	0.46	0.48	0.49
B_6C_2 -[C2&C3]	-2.37	-1.75	-0.95	-1.62	-2.05	0.36	0.66	0.47
B_6C_2 -R-[C5&C6]	-2.05	-2.49	-1.09	-2.24	-2.85	0.59	0.32	0.66

(top) ab initio hopping matrix elements (in eV) for borophene and C-doped borophene obtained from Wannier functions. Conventions for labeling of the hopping matrix elements are given in Fig. 2a. (bottom) Renormalized parameters of Fig. 2c. ζ_y is the tilt parameter and k_D/k_Y quantifies the location of Dirac node.

ignore here. Green/red hopping processes are associated with the second/third neighbors of the honeycomb backbone that originate from the corresponding atomic process t_{ij} of panel (a) via the renormalization.

Let us see how the atomic processes t_{ij} in Fig. 2a are related to the effective hopping processes in Fig. 2c³⁴. For example consider

the simplest third neighbor R sites 2 and 3 of adjacent unit cells in Fig. 2a that becomes possible via atomic hoppings t_{27} and t_{37} of Fig. 2a. The hopping process via the R site 7 is depicted in Fig. 3a. Assuming an on-site energy offset 2Δ for the R sites with respect to I site, an electron starting at the site 2 virtually hops to R site 7 and then returns to low-energy sector at site 3. Through this

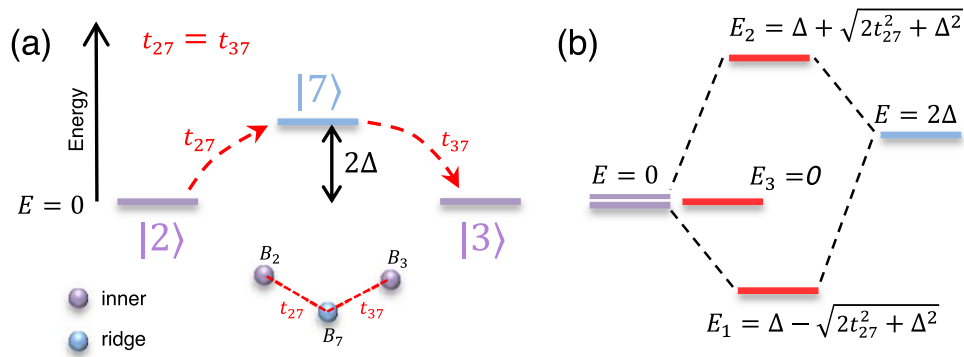


Fig. 3 Effective 3rd neighbor hopping t^P via the “stepping stone” sites. **a** Virtual hopping via the ridge site 7 generates an effective hopping t^P between 2 and its third neighbor site 3—i.e. site 3 in the adjacent unit cell in Fig. 2(a). **b** The odd parity combination of 2 and 3 remains decoupled, but the even parity combination hybridizes with ridge site to gain energy. 2Δ is difference of atomic on-site energy.

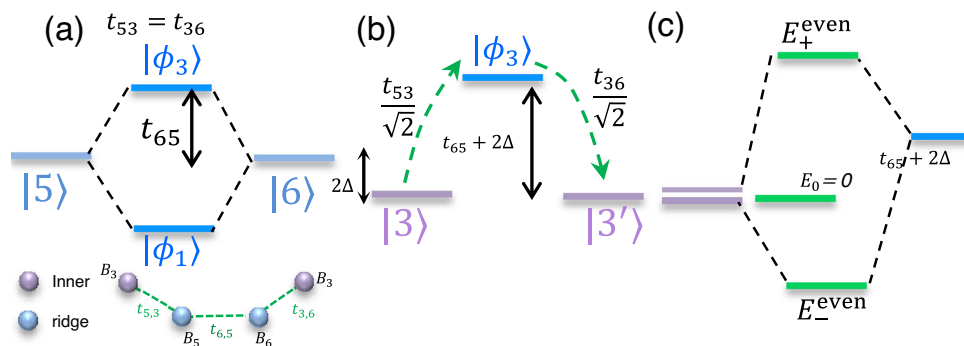


Fig. 4 Effective 2nd neighbor hopping t via “stepping stone” sites. **a** Formation of bonding $|\phi_1\rangle$ and anti-bonding $|\phi_2\rangle$ orbitals between the ridge atoms 5 and 6. **b** Effective hopping \tilde{t} between second neighbor inner sites 3 and 3' can be formed by virtual hopping via the anti-bonding orbital $|\phi_3\rangle$ of two ridge atoms. 2Δ is difference of atomic on-site energy. E_0 is atomic on-site energy of |3> and |3'> and it is set to zero. **c** Energy diagram after the formation of molecular states which connect B3 to one of its successive third nearest neighbors through antibonding orbitals.

process it gains the following energy (see Fig. 3b)

$$t^P = \Delta - \sqrt{2t_{27}^2 + \Delta^2} < 0, \quad (1)$$

even in the limit of $\Delta \rightarrow 0$ this gives an energy lowering $-\sqrt{2}|t_{27}|$ that can be regarded as effective hopping between the third neighbor sites 2 and 3 of the I sublattice. To intuitively understand this formula, note that in the absence of the I site, $t_{27} = t_{37} = 0$, and hence both even and odd combinations of third neighbor atomic orbitals $|2\rangle \pm |3\rangle$ remain inert. But once the inner site is present, the atomic hopping t_{27} causes a coupling of $|7\rangle$ with the even-parity state $|2\rangle + |3\rangle$, leaving the odd parity state $|2\rangle - |3\rangle$ decoupled at zero energy. The coupling with the even parity combination provides a channel to lower the energy given by the effective hopping in Eq. (1). Furthermore, in the limit of $\Delta \gg |t_{27}|$ the above formula reduces to the perturbatively appealing form $-2t_{27}^2/\Delta$. For pedagogical details of the above computation, please refer to Supplementary Note 3.

As a second example, consider the I site 3 in Fig. 2a and the same site in the unit cell above it (that we denote by 3'). These sites will be second neighbor on the coarse grained lattice and there are two hopping pathways $3 \rightarrow 6 \rightarrow 5 \rightarrow 3'$ and $3 \rightarrow 8 \rightarrow 7 \rightarrow 3'$ connecting them that are denoted by light and dark green dashed lines in Fig. 2a. The process of the calculation of the effective hopping amplitude $3 \rightarrow 3'$ is similar for the above two paths. So we focus on the first one. In principle one must consider the energy gained by the lowest molecular orbitals formed by the above chain of sites. This has been done in Supplementary Note 3. The end result allows for a nice and intuitive interpretation depicted in Fig. 4(a–c): First,

due to hopping t_{65} , the R sites 5 and 6 form bonding and anti-bonding molecular orbitals denoted by $|\phi_1\rangle$ and $|\phi_2\rangle$ in Fig. 4a. Then as depicted in panel (b), an electron gains energy by virtually hopping via the anti-bonding orbital $|\phi_3\rangle$ whose energy is now offset by $t_{65} + 2\Delta$. The hoppings connecting site 3 and 3' to $|\phi_3\rangle$ are $t_{65}/\sqrt{2}$ where the $\sqrt{2}$ factor comes from the normalization $|\phi_3\rangle = (|\phi_5\rangle - \phi_6)/\sqrt{2}$. In the final step as shown in Fig. 4c, the even-parity combination of |3> and |3'> is mixed with $|\phi_3\rangle$ to give an energy gain $E_{-}^{\text{even}} = (t_{56}/2 + \Delta) - \sqrt{(t_{56}/2 + \Delta)^2 + t_{63}^2}$. A similar contribution arises from the second path. Adding the two contributions we obtain the total renormalized hopping \tilde{t} of Fig. 2c as

$$\tilde{t} = \frac{t_{56} + t_{87} + 4\Delta}{2} - \sqrt{\left(\frac{t_{56}}{2} + \Delta\right)^2 + t_{63}^2} - \sqrt{\left(\frac{t_{87}}{2} + \Delta\right)^2 + t_{73}^2} \quad (2)$$

in the above formula, the hopping parameters t_{65} and t_{87} are dominantly contributed by the p_x and p_z orbitals as the intensities of the p_x, p_z orbitals in the second row of Fig. 1e are dominant, while p_y orbital is faint. Similarly the two other renormalized hopping parameters t^x and \tilde{t} can be computed. For details please refer to Supplementary Information (SI), where we have shown that the elimination of higher energy states actually corresponds to the above simple molecular orbital analysis.

This is how the renormalized parameters of the coarse grained honeycomb graph model in the bottom part of Table 1 are computed from the ab initio data of the top part of the table. Note that if instead of 8Pmmn structure, we had a simple honeycomb lattice (such as in graphene), such a large values of second or third neighbor hopping given in Table 1 would be unthinkable as hopping between the atomic orbitals exponentially decays with distance. Therefore the virtual hopping via the ridge sites attaches a great importance to them as providers of channels for energy gain and ultimate formation of renormalized hoppings on a coarse grained lattice of inner sites. Furthermore, this is an example of how the molecular orbital play a significant role in the formation of longer range hoppings on the decimated 8 Pmmn lattice.

Effective coarse-grained model. Now that we have identified the p_z orbitals residing at the inner sites as the low-energy degrees of freedom, and have computed various renormalized hoppings between second and third neighbors, we are ready to write down a physically clear low-energy effective model that will straightforwardly demonstrate how the renormalized parameters t^p , t^x , \tilde{t} and \bar{t} can provide information about the position and the amount of the tilt.

The first neighbor hoppings denoted by black arrows in Fig. 2c are present even when there are no R sites. In the two-dimensional Hilbert space of A and B sublattice of such a honeycomb lattice, these hoppings contribute the usual off-diagonal term $F_0(\mathbf{k}) = -\sum_{\alpha=1,2,3} e^{i\mathbf{k}\cdot\delta_\alpha}$ to the Bloch Hamiltonian, where the sum over α runs over three first neighbors in Fig. 2c. This is responsible for the formation of a pair of upright Dirac cones similar to graphene. Slight anisotropy of the honeycomb

lattice of R sites will amount to a shift in the location of the Dirac cone³² which is irrelevant for our purposes. For concrete calculations, we assume a regular effective honeycomb lattice of bond length a for which the Dirac nodes in the rhombus BZ are at $K_0^\pm = \frac{2\pi}{3a}(\hat{i} \pm \frac{1}{\sqrt{3}}\hat{j})$ ²³.

Next let us consider the third neighbor hoppings denoted by red arrows in Fig. 2c labeled by t^p (superscript “p” for pseudo, as they give rise to pseudogauge fields that shift the location of the Dirac node in opposite directions) and t^x (superscript “x” to emphasize the role of p_x orbitals of R sites). They contribute another off-diagonal term given by $F_{xp}(\mathbf{k}) = t^p e^{2iak_x} + 2t^x e^{-iak_x} \cos(\sqrt{3}ak_y)$ to the Bloch Hamiltonian. Expanding this form factor around the Dirac nodes K_0^\pm above, gives rise to (i) a shift $\Delta k_D = 2(t^p - t^x)/(\mp 3at \pm at^x)$ of the Dirac node, where t is the nearest neighbor hopping (assumed to be 1) and (ii) anisotropy in the Fermi velocity given by $v_{F_x} \rightarrow v_{F_x}(1 + \frac{4t^p + 2t^x}{3t})$ and $v_{F_y} \rightarrow v_{F_y}(1 - \frac{6t^x}{3t})$. Therefore the first and third neighbor hoppings establish the location of the (still upright) Dirac cone and determine its Fermi anisotropic velocities.

Now let us focus on the second neighbors (green arrows) in Fig. 2c that are the root cause of the tilt formation⁷. Since these hoppings are driven via virtual hopping through different arrangements of molecular orbitals, there are two types of them denoted by solid (\bar{t}) and dashed (\tilde{t}) green lines. These hoppings being second neighbor, connect two atoms on the same sublattice, and therefore contribute to the diagonal terms, namely AA and BB components of the effective 2×2 Hamiltonian matrix. Among the matrices σ_μ with $\mu = 0 \dots 3$, only σ_0 and σ_z can contribute diagonal terms. So now one has to decide whether these diagonal terms come with the same sign (σ_0 term \rightarrow tilt) or opposite signs

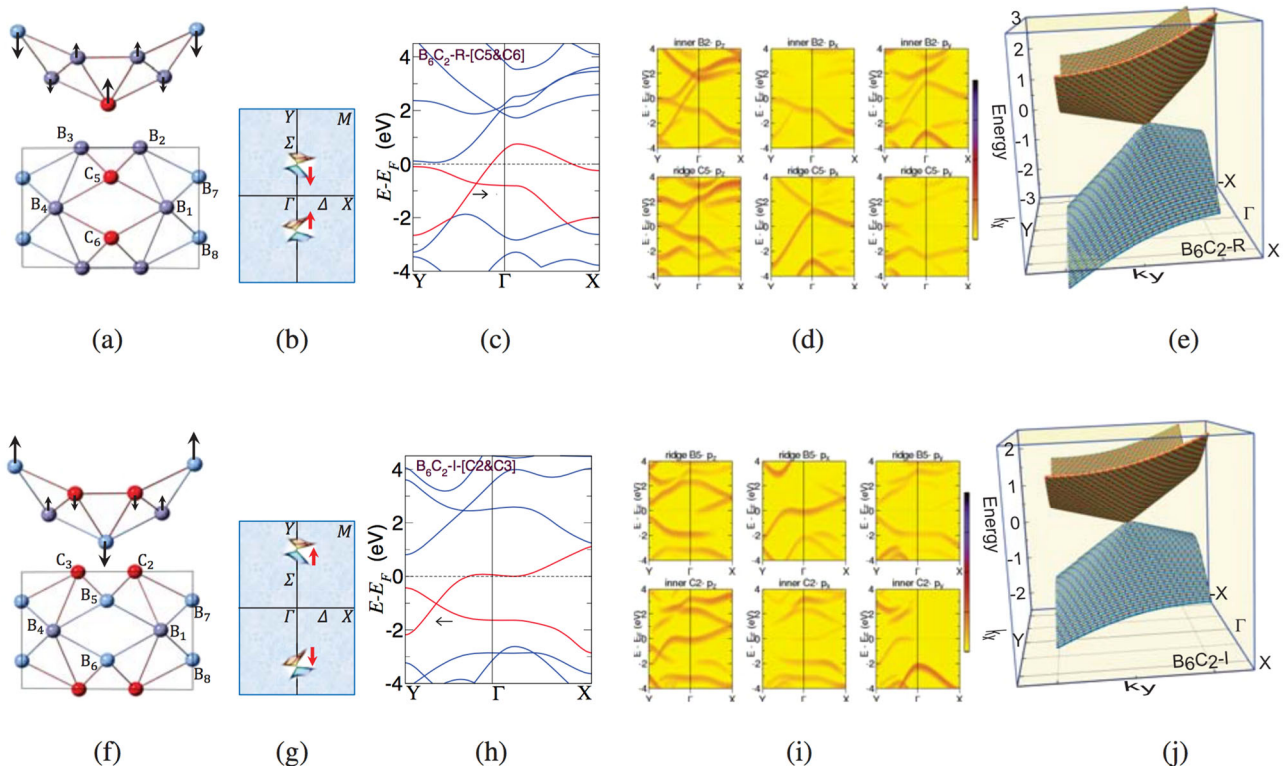


Fig. 5 Manipulation of the tilt of Dirac cone by carbon substitution in 8 Pmmn borophene. **a** Top view of crystal structure of $B_6C_2\text{-R-[C5\&C6]}$ and **b** its Brillouin zone. The red circles denote carbon atoms. **c** Density functional theory with Perdew-Burke-Ernzerhof (DFT-PBE) band structure of $B_6C_2\text{-R-[C5\&C6]}$, **d** its orbital-projected band structures for two atoms and **(e)** its three dimensional reconstruction. **f-j** The same as **(a-e)** for $B_6C_2\text{-l-[C2\&C3]}$. The horizontal arrows in panels **c** and **h** indicate the direction of the displacement of the Dirac node with respect to the parent B_8 . The vertical arrows in **a** and **f** show the direction of movement of the lattice sites upon carbon substitution.

(σ_z term \rightarrow gap). There are two ways to see that this term must be proportional to the σ_z : (i) Analysis of the irreducible representations and compatibility relations of the original 8Pmmn structure in Fig. 1d shows that the crossing of the red bands is protected by the glide elements of the 8Pmmn lattice (see Supplementary Note 1 for details). Since the effective theory has to obey this protection against gap opening, the σ_z term is ruled out. (ii) Consider the renormalized lattice itself and focus on the solid green line in Fig. 2c. If the hopping between 1 and 3 in Fig. 1a contributes to AA term, the hopping between 2 and 4 contribute to BB term. Both these contributions arise from the p_z orbitals of these atoms via intermediate hopping through p_z orbital of atom 5. Apparently for p_z orbitals the “northwest” ($1 \rightarrow 5 \rightarrow 3$) and “northeast” ($4 \rightarrow 5 \rightarrow 2$) hoppings are identical. Similar arguments holds for the dashed green line in Fig. 2c. In this case AA (BB) term is generated by $3 \rightarrow 6 \rightarrow 5 \rightarrow 3$ ($2 \rightarrow 6 \rightarrow 5 \rightarrow 2$) path. Again the p_x orbitals of the 5, 6 atoms symmetrically connect $3 \rightarrow 3'$ and $2 \rightarrow 2'$ (remember $3'$ is the same as 3 but in adjacent unit cell. Similarly for $2'$), thereby giving identical AA and BB terms in the effective Hamiltonian.

Therefore the effective Hamiltonian becomes (for more details see Supplementary Note 2)

$$H_{\text{eff}}(\mathbf{k}) = \begin{pmatrix} f_{\text{tilt}}(\mathbf{k}) & f(\mathbf{k}) \\ f^*(\mathbf{k}) & f_{\text{tilt}}(\mathbf{k}) \end{pmatrix}, f(\mathbf{k}) = F_{\text{xp}}(\mathbf{k}) + F_0(\mathbf{k}), \quad (3)$$

$$f_{\text{tilt}}(\mathbf{k}) = 2\tilde{t} \cos(\sqrt{3}ak_y) + 4\bar{t} \cos(3ak_x/2) \cos(\sqrt{3}ak_y/2).$$

Taylor expanding the diagonal f_{tilt} term around the Dirac node formed by off-diagonal terms gives,

$$\zeta_x = 0, \quad \zeta_y = \pm 2 \frac{\tilde{t} - \bar{t}}{t}, \quad (4)$$

where \pm corresponds to the valley around which the expansion is performed.

The above equation indicates that the tilt arises from the difference of the second neighbor hoppings \tilde{t} and \bar{t} that in turn are generated via the p_x and p_z orbitals of the R atoms. An immediate suggestion of the above model is to (partially) replace the R-site boron atoms by carbon atoms to see whether the tilt is changed or not. In Fig. 5(a–j) we have replaced two of the boron atoms with C atoms. For this purpose there are two choices: (i) To place a carbon dimer on the R sites as in the panel (a) or (ii) to place the carbon atoms in the I sites as in panel (f). The results are summarized in Table 1. For case (i), the location of the Dirac node is shifted towards the Γ point and its tilt increases. Placing carbon atoms in the R sites shifts the 5 and 6 sites to higher energies, thereby generating larger \tilde{t} and \bar{t} (see Table 1) that ultimately increases the tilt from the $\zeta_y = 0.46$ of the pristine borophene to $\zeta_y = 0.59$ in $B_6C_2\text{-R-[C5\&C6]}$. Our picture provides also a way to decrease the tilt parameter. In this case, the hybridization of the p_z orbitals of sites 2, 3 with the R sites (5, 6) reduces as in Table 1 and hence the resulting \bar{t} and likewise \tilde{t} are scaled down, thereby reducing the tilt to 0.36 in $B_6C_2\text{-I-[C2\&C3]}$. The above values of the tilt ζ_y are calculated based on Eq. (4) and as detailed in Supplementary Note 4, are in good agreement with the corresponding values directly extracted from DFT bands.

As shown in Supplementary Fig. 6 of Supplementary Note 4, for doping of two carbon atoms into the structural unit of B_8 , the R-site configurations (c) and (k) have the lower energy than all other configurations, with staggered configuration (k) having slightly lower energy than (c). For a perfect (translationally invariant) doping of two C into the 8Pmmn borophene structure, the changes in the tilt are discrete. However, the concentration of C atoms can be continuously varied. Statistical averaging for a concentration x that continuously varies between 0 and 2/8 is

expected to generate a continuously varying tilt. The dominant configurations will be the R-site dimers and staggered R-site configurations of panel (c) and (k) of Supplementary Fig. 6. The lack of perfect backscattering of Dirac electrons is expected to protect the Dirac cone against the Anderson localization.

Conclusions

Based on our ab initio calculations, we have identified the p_z orbitals of the I sites as real space sublattice on which the low-energy degrees of freedom in 8Pmmn lattice reside. The effective hoppings between these sites are obtained via renormalization that encodes the virtual hopping via R-sites (Supplementary Note 5). This gives a physically clear picture of the formation of the tilt in two-dimensional Dirac cone of 8Pmmn borophene. In our picture, tilt arises from a competition between two renormalized hoppings \tilde{t} and \bar{t} between the second neighbor I-sites. The former involves virtual hopping via two R sites (and $2p_x$ orbitals of the R sites), while the latter involves one R site. This builds in a natural difference between \bar{t} and \tilde{t} . That is why the pristine borophene has a substantial tilting. Within this picture it is natural to expect that replacing the ridge (inner) atoms by C increase (decreases) the tilt. The rest of the effective hoppings determine the location of the (protected) Dirac node and the anisotropy in the Fermi velocity.

The logic of our work can be applied to other SGs to discover more GQM within a class of 2D materials that afford to provide a “parent” upright Dirac cone: Molecular orbitals in certain SGs can mediate longer range hoppings on a backbone lattice of Dirac fermions by promoting it to appropriate graph. The resulting graph in turn deforms the Minkowski spacetime of the Dirac fermions into a metric involving spatio-temporal elements. The ability to tune the tilt parameter is tantamount to controllability of the ensuing solid-state spacetime structure that emerges at long distances. Dirac materials subject to “gravitational” (i.e. geometric) disorder^{35,36} find their salient materialization in the present context when the carbon is randomly substituted for boron. Assuming a doping fraction x of carbon atoms that can be continuously tuned, the most favorable configurations for the C atoms are R-site dimers and staggered R-site (Supplementary Fig. 6c, and k, respectively). Random substitutions of this form are expected to lead to continuous variation of tilt as a function of x . The absence of backscattering for Dirac fermions protects it against Anderson localization³⁷.

The relation between certain graphs and their continuum limit as space geometries is well known^{38–40}. In the present context, each edge of the graph is associated with a hopping energy (frequency) scale. This is how space and time are mingled and a spacetime geometry (rather than space geometry) emerges at long distances. This is how a solid-state platform can promote a simple lattice that supports Dirac fermions into a rich graph where vierbeins can be attached to the Dirac fermions^{41,42}. This enriches the physics of Dirac materials and promotes them to GQMs where a variety of spacetime geometries can be fabricated that might not even have any analogue in the cosmos. On the 2D materials side, there will be a plenty of room to explore the effects of “geometric” forces or even synthesise non-Abelian gauge fields⁴³ that are likely to lead to better control in electronic/optical devices, as the effects of spacetime curvature^{44,45} can be much stronger GQMs. Furthermore, the geometry of our emergent spacetime in GQMs roots in the Coulomb forces that are much stronger than the gravitational forces and unlike the gravity, the Coulomb forces can be both attractive and repulsive. Therefore the geometric structure of GQMs seems to be much richer than the Einstein’s gravity. In three dimensional tilted Dirac/Weyl fermions the resulting geometric theory can be even more

interesting: The fermions in such materials are chiral and hence a chiral geometric theory can be relevant to GQM. The developments in GQMs will allow us to emulate aspects of spacetime geometry that is not easily accessible in the cosmos. GQMs have a potential to equip Dirac fermions with types of vielbeins⁴¹ that are beyond the spatial vielbeins of the strain/dislocation paradigm⁴².

Methods

For DFT calculation we have used pseudopotential Quantum Espresso code based on plane wave basis set within the generalized gradient approximation in the Perdew-Burke-Ernzerhof (PBE) parameterization⁴⁶. Simulation of borophene rectangular unit cells is based on the slab model having a 25 Å vacuum separating slabs. We also consider monolayer of 8Pmmn structure, where some of the B atoms are substituted by C atoms in the form of $B_{8-x}C_x$ ($x = 0, 1, 2$). The obtained structural properties after the ionic relaxations such as lattice parameters, x , y , and z component of the B and C atoms in crystal coordinates are shown in Supplementary Table II of SI for pure borophene (B_8) and C-doped systems $B_{8-x}C_x$. The uniform k -point grids of $24 \times 24 \times 1$ are used for the self-consistent field calculations of all systems. The Kinetic energy cut-offs for the wavefunctions and the charge density are 850 and 8500 eV, respectively. For each system, the Broyden-Fletcher-Goldfarb-Shanno quasi-Newton algorithm is used to relax the internal coordinates of the B and C atoms and possible distortions with convergence threshold on forces for ionic minimization as small as 10^{-4} eVÅ⁻¹. Also the generation of new edges on the honeycomb graph is based on the standard molecular orbital theory that can also be formulated in the language of the renormalization. The protection of the Dirac node can be directly seen by looking into irreducible representation of the little groups. The full pedagogical details of the above procedure is presented in Supplementary Notes 4 and 5 of the SI.

Data availability

The details of calculations that support the findings of this study are available in the supplementary information (SI). Any other details if required, are available from the corresponding authors upon request.

Received: 29 November 2021; Accepted: 27 February 2023;

Published online: 15 March 2023

References

- Inui, T., Tanabe, Y. & Onodera, Y. Space groups. In *Group Theory and Its Applications in Physics*, 234–258 (Springer Berlin Heidelberg, 1990). https://doi.org/10.1007/978-3-642-80021-4_11.
- Girvin, S. M. & Yang, K. *Modern Condensed Matter Physics* (Cambridge University Press, 2019). <https://doi.org/10.1017/9781316480649>.
- Ryder, L. H. *Quantum Field Theory* (Cambridge University Press, 1996). <https://doi.org/10.1017/cbo9780511813900>.
- Bradlyn, B. et al. Beyond dirac and weyl fermions: Unconventional quasiparticles in conventional crystals. *Science* **353**, aaf5037 (2016).
- Ando, T. Zero-mode anomalies of massless dirac electron in graphene. *J. Appl. Phys.* **109**, 102401 (2011).
- Tajima, N., Sugawara, S., Tamura, M., Nishio, Y. & Kajita, K. Electronic phases in an organic conductor α -(BEDT-TTF)₂I₃: Ultra narrow gap semiconductor, superconductor, metal, and charge-ordered insulator. *J. Phys. Soc. Jpn.* **75**, 051010 (2006).
- Goerbig, M. O., Fuchs, J.-N., Montambaux, G. & Piéchon, F. Tilted anisotropic dirac cones in quinoid-type graphene and α -(BEDT-TTF)₂I₃. *Phys. Rev. B* **78**, 045415 (2008).
- Kajita, K., Nishio, Y., Tajima, N., Suzumura, Y. & Kobayashi, A. Molecular dirac fermion systems — theoretical and experimental approaches —. *J. Phys. Soc. Jpn.* **83**, 072002 (2014).
- Farajollahpour, T., Faraei, Z. & Jafari, S. A. *Solid-state platform for space-time engineering: The 8pmmn borophene sheet*. Physical Review B **99** (2019). <https://doi.org/10.1103/physrevb.99.235150>.
- Jalali-Mola, Z. & Jafari, S. A. Polarization tensor for tilted dirac fermion materials: covariance in deformed minkowski spacetime. *Phys. Rev. B* **100**, 075113 (2019).
- Verma, S., Mawrie, A. & Ghosh, T. K. Effect of electron-hole asymmetry on optical conductivity in 8-pmmn borophene. *Phys. Rev. B* **96**, 155418 (2017).
- Jafari, S. A. Electric field assisted amplification of magnetic fields in tilted dirac cone systems. *Phys. Rev. B* **100**, 045144 (2019).
- Westström, A. & Ojanen, T. Designer curved-space geometry for relativistic fermions in weyl metamaterials. *Phys. Rev. X* **7**, 041026 (2017).
- Liang, L. & Ojanen, T. Curved spacetime theory of inhomogeneous weyl materials. *Phys. Rev. Res.* **1**, 032006 (2019).
- Volovik, G. E. Black hole and hawking radiation by type-ii weyl fermions. *JETP Lett.* **104**, 645–648 (2016).
- Volovik, G. E. Exotic lifshitz transitions in topological materials. *Phys.-Uspekhi* **61**, 89–98 (2018).
- Nissinen, J. & Volovik, G. E. Type-iii and iv interacting weyl points. *JETP Lett.* **105**, 447–452 (2017).
- Mohajerani, A., Faraei, Z. & Jafari, S. A. Fast nuclear spin relaxation rates in tilted cone Weyl semimetals: redshift factors from Korringa relation. *Journal of Physics: Condensed Matter* **33**, 215603 (2021).
- Bradley, C. & Cracknell, A. *The mathematical theory of symmetry in solids: representation theory for point groups and space groups* (Oxford University Press, 2010).
- Krowne, C. M. & Sha, X. Atomic structural and electronic bandstructure calculations for borophene. *Mater. Res. Express* **8**, 026301 (2021).
- Feng, B. et al. Dirac fermions in borophene. *Phys. Rev. Lett.* **118**, 096401 (2017).
- Motavassal, A. & Jafari, S. A. Circuit realization of a tilted dirac cone: platform for fabrication of curved spacetime geometry on a chip. *Phys. Rev. B* **104**, L241108 (2021).
- Katsnelson, M. I. *Graphene* (Cambridge University Press, 2012). <https://doi.org/10.1017/cbo9781139031080>.
- Zhou, X.-F. et al. Semimetallic two-dimensional boron allotrope with massless dirac fermions. *Phys. Rev. Lett.* **112**, 085502 (2014).
- Lopez-Bezanilla, A. & Littlewood, P. B. Electronic properties of 8-pmmn borophene. *Phys. Rev. B* **93**, 241405 (2016).
- Kittel, C. *Quantum Theory of Solids* (John Wiley & Sons, New York, 1987), 2nd edn.
- Fan, X., Ma, D., Fu, B., Liu, C.-C. & Yao, Y. Cats-cradle-like dirac semimetals in layer groups with multiple screw axes: Application to two-dimensional borophene and borophane. *Phys. Rev. B* **98** (2018). <https://doi.org/10.1103/physrevb.98.195437>.
- Yekta, Y., Hadipour, H. & Jafari, S. A. Tunning the tilt of a dirac cone by atomic manipulations: application to 8pmmn borophene (2021). *arXiv* <https://arxiv.org/abs/2108.08183>.
- Mostofi, A. A. et al. An updated version of wannier90: A tool for obtaining maximally-localised wannier functions. *Comput. Phys. Commun.* **185**, 2309–2310 (2014).
- Freimuth, F., Mokrousov, Y., Wortmann, D., Heinze, S. & Blügel, S. Maximally localized wannier functions within the flapw formalism. *Phys. Rev. B* **78**, 035120 (2008).
- Anderson, P. W. *Basic Notions of Condensed Matter Physics* (CRC Press, 2018). <https://doi.org/10.4324/9780429494116>.
- Vozmediano, M., Katsnelson, M. & Guinea, F. Gauge fields in graphene. *Phys. Rep.* **496**, 109–148 (2010).
- Krowne, C. M. Introduction to examination of 2d hexagonal band structure from a nanoscale perspective for use in electronic transport devices. In *Advances in Imaging and Electron Physics*, 1–6 (Elsevier, 2019). <https://doi.org/10.1016/bs.aiep.2019.01.001>.
- Grosso, G. & Paravicini, G. P. *Solid State Physics* (Elsevier, 2000). <https://doi.org/10.1016/b978-0-12-304460-0.x5000-2>.
- Ghorashi, S. A. A., Karcher, J. F., Davis, S. M. & Foster, M. S. Criticality across the energy spectrum from random artificial gravitational lensing in two-dimensional dirac superconductors. *Phys. Rev. B* **101**, 214521 (2020).
- Davis, S. M. & Foster, M. S. Geodesic geometry of 2+1-D Dirac materials subject to artificial, quenched gravitational singularities. *SciPost Phys.* **12**, 204 (2022).
- Ando, T. Physics of graphene. *Prog. Theor. Phys. Suppl.* **176**, 203–226 (2008).
- Boettcher, I., Bienias, P., Belyansky, R., Kollár, A. J. & Gorshkov, A. V. Quantum simulation of hyperbolic space with circuit quantum electrodynamics: From graphs to geometry. *Phys. Rev. A* **102** (2020). <https://doi.org/10.1103/physreva.102.032208>.
- Baek, S. K., Minnhagen, P. & Kim, B. J. Percolation on hyperbolic lattices. *Phys. Rev. E* **79** (2009). <https://doi.org/10.1103/physreve.79.011124>.
- Kollár, A. J., Fitzpatrick, M. & Houck, A. A. Hyperbolic lattices in circuit quantum electrodynamics. *Nature* **571**, 45–50 (2019).
- Yepez, J. Einstein's vierbein field theory of curved space (2011). *arXiv* <https://arxiv.org/abs/1106.2037>.
- Hughes, T. L., Leigh, R. G. & Parrikar, O. Torsional anomalies, hall viscosity, and bulk-boundary correspondence in topological states. *Phys. Rev. D* **88** (2013). <https://doi.org/10.1103/physrevd.88.025040>.
- Farajollahpour, T. & Jafari, S. A. Synthetic non-abelian gauge fields and gravitomagnetic effects in tilted dirac cone systems2 (2020). <https://doi.org/10.1103/physrevresearch.2.023410>.

44. Exirifard, Q., Culf, E. & Karimi, E. Towards communication in a curved spacetime geometry. *Commun. Phys.* 4 (2021). <https://doi.org/10.1038/s42005-021-00671-8>.
45. Exirifard, Q. & Karimi, E. Schrödinger equation in a general curved spacetime geometry. *International Journal of Modern Physics D* 33, 2250018 (2022).
46. Perdew, J. P., Burke, K. & Ernzerhof, M. Generalized gradient approximation made simple. *Phys. Rev. Lett.* 77, 3865–3868 (1996).

Acknowledgements

S. A. J. was supported by grant No. G960214 from the research deputy of Sharif University of Technology and Iran Science Elites Federation (ISEF). We thank Prof. Dr. Reza Mansouri for continuous support of our line of research on solid-state spacetimes and enlightening discussions on spacetime aspects.

Author contributions

S.A.J. conceived the project. H.H. supervised DFT calculations. Y.Y. performed the electronic structure calculations. All authors discussed the results and shaped the message of the paper. The paper was written by H.H. and S.A.J.

Competing interests

The authors declare no competing interests.

Additional information

Supplementary information The online version contains supplementary material available at <https://doi.org/10.1038/s42005-023-01161-9>.

Correspondence and requests for materials should be addressed to Seyed Akbar Jafari.

Peer review information *Communications Physics* thanks Chengcheng Liu and the other, anonymous, reviewer(s) for their contribution to the peer review of this work. Primary Handling Editor: Aldo Isidori.

Reprints and permission information is available at <http://www.nature.com/reprints>

Publisher's note Springer Nature remains neutral with regard to jurisdictional claims in published maps and institutional affiliations.



Open Access This article is licensed under a Creative Commons Attribution 4.0 International License, which permits use, sharing, adaptation, distribution and reproduction in any medium or format, as long as you give appropriate credit to the original author(s) and the source, provide a link to the Creative Commons license, and indicate if changes were made. The images or other third party material in this article are included in the article's Creative Commons license, unless indicated otherwise in a credit line to the material. If material is not included in the article's Creative Commons license and your intended use is not permitted by statutory regulation or exceeds the permitted use, you will need to obtain permission directly from the copyright holder. To view a copy of this license, visit <http://creativecommons.org/licenses/by/4.0/>.

© The Author(s) 2023